

## CROSS-CORRELATION BETWEEN THE CMB LENSING POTENTIAL MEASURED BY *PLANCK* AND HIGH-Z SUB-MM GALAXIES DETECTED BY THE *HERSCHEL*-ATLAS SURVEY

F. BIANCHINI<sup>1,12</sup>, P. BIELEWICZ<sup>1</sup>, A. LAPI<sup>2,1,12,13</sup>, J. GONZALEZ-NUENO<sup>3</sup>, C. BACCIGALUPI<sup>1,12</sup>, G. DE ZOTTI<sup>4,1</sup>, L. DANESE<sup>1</sup>, N. BOURNE<sup>5</sup>, A. COORAY<sup>6</sup>, L. DUNNE<sup>7,5</sup>, S. DYE<sup>8</sup>, S. EALES<sup>9</sup>, R. IVISON<sup>5,10</sup>, S. MADDOX<sup>7,5</sup>, M. NEGRELLO<sup>4</sup>, D. SCOTT<sup>11</sup>, M. W. L. SMITH<sup>9</sup>, E. VALIANTE<sup>9</sup>

*Draft version May 15, 2022*

### ABSTRACT

We present the first measurement of the correlation between the map of the CMB lensing potential derived from the *Planck* nominal mission data and  $z \gtrsim 1.5$  galaxies detected by the *Herschel*-ATLAS

(H-ATLAS) survey covering about 600 deg<sup>2</sup>, i.e. about 1.4% of the sky. We reject the no CMB lensing-galaxy correlation hypothesis at a 20 $\sigma$  significance, checking the result by performing a number of null tests. The significance of the detection of the theoretically expected cross-correlation signal is found to be 10 $\sigma$ . The galaxy bias parameter,  $b$ , derived from a joint analysis of the cross-power spectrum and of the auto-power spectrum of the galaxy density contrast is found to be  $b = 2.80^{+0.12}_{-0.11}$ , consistent with earlier estimates for H-ATLAS galaxies at similar redshifts. On the other hand, the amplitude of the cross-correlation is found to be a factor  $1.62 \pm 0.16$  higher than expected from the standard model and also found by cross-correlation analyses with other tracers of the large-scale structure. The enhancement due to lensing magnification can account for only a fraction of the excess cross-correlation signal. We suggest that part of it may be due to an incomplete removal of the contamination of the CIB, that includes the H-ATLAS sources we are cross-correlating with. In any case, the highly significant detection reported here using a catalog covering only 1.4% of the sky demonstrates the potential of CMB lensing correlations with sub-mm surveys.

*Keywords:* galaxies: high-redshift, cosmic background radiation, gravitational lensing: weak, methods: data analysis, cosmology: observations

### 1. INTRODUCTION

Cosmological observations carried out in the last two decades have enabled the establishment of the standard cosmological model. In this picture, observed galaxies form in matter over-densities that are the result of the growth, driven by gravitational instabilities in an expanding Universe, of primordial inhomogeneities generated during an inflationary epoch. A picture of primordial inhomogeneities at an early stage of their evolution is

provided by observations of the cosmic microwave background (CMB) anisotropy.

However, this picture is to some extent distorted by interactions of the CMB photons with matter inhomogeneities encountered during their travel from the last-scattering surface to the observer. On the other hand, these effects are a useful source of information on the large-scale structure of the Universe. One of these effects is gravitational lensing, causing small but coherent deflections of the observed CMB temperature and polarisation anisotropies, with a typical amplitude of 2'. Specific statistical signatures of lensing enable the reconstruction of the gravitational potential integrated along the line of sight from observed CMB maps (Hu & Okamoto 2002; Hirata & Seljak 2003).

In recent years CMB lensing has been measured in a number of CMB experiments. The first detections were made via cross-correlations with large-scale structure probed by galaxy surveys (Smith et al. 2007; Hirata et al. 2008; Feng et al. 2012; Bleem et al. 2012; Sherwin et al. 2012; Geach et al. 2013). The higher sensitivity and resolution of recent CMB instruments, such as the Atacama Cosmology Telescope (ACT), the South Pole Telescope (SPT) and *Planck*, have enabled an internal detection of lensing using CMB data alone (Das et al. 2011; Keisler et al. 2011; Das et al. 2014; van Engelen et al. 2012); the measurement with the highest signal-to-noise ratio, around 25 $\sigma$ , was reported last year by the *Planck* team (Planck Collaboration XVII 2013).

As already mentioned, the CMB lensing potential is an *integrated* measure of the matter distribution in the Universe, up to the last-scattering surface. As illustrated

fbianchini@sissa.it

<sup>1</sup> Astrophysics Sector, SISSA, Via Bonomea 265, I-34136 Trieste, Italy; fbianchini@sissa.it

<sup>2</sup> Dipartimento di Fisica, Università “Tor Vergata”, Via della Ricerca Scientifica 1, I-00133 Roma, Italy

<sup>3</sup> Inst. de Fisica de Cantabria (CSIC-UC), Avda. los Castros s/n, 39005 Santander, Spain

<sup>4</sup> INAF - Osservatorio Astronomico di Padova, Vicolo dell'Osservatorio 5, I-35122 Padova, Italy

<sup>5</sup> Institute for Astronomy, University of Edinburgh, Royal Observatory, Blackford Hill, Edinburgh EH9 3HJ, UK

<sup>6</sup> Department of Physics and Astronomy, University of California Irvine CA 92697 USA

<sup>7</sup> Department of Physics and Astronomy, University of Canterbury, Private Bag 4800, Christchurch, 8140, New Zealand

<sup>8</sup> School of Physics and Astronomy, University of Nottingham, University Park, Nottingham, NG7 2RD, UK

<sup>9</sup> School of Physics and Astronomy, Cardiff University, Queens Buildings, The Parade, Cardiff CF24 3AA, UK

<sup>10</sup> European Southern Observatory, Karl Schwarzschild Strasse 2, Garching, Germany

<sup>11</sup> Department of Physics & Astronomy, University of British Columbia, Vancouver, BC V6T 1Z1, Canada

<sup>12</sup> INFN - Sezione di Trieste, Via Valerio 2, I-34127 Trieste, Italy

<sup>13</sup> INAF - Osservatorio Astronomico di Trieste, via Tiepolo 11, 34131, Trieste, Italy

by Fig. 1, it has a broad kernel, peaking at  $z \simeq 2$  but slowly varying from  $z \simeq 1$  to  $z \gtrsim 4$ . The study of cross-correlations with other tracers of large scale structure covering narrow redshift ranges allows us to reconstruct the dynamics and spatial distribution of the cosmological gravitational potentials. This can tighten tests of the time evolution of dark matter density fluctuations and through that give constraints on the dynamics of the dark energy at the onset of cosmic acceleration. Since the cross-correlations measure the average lensing signal from the dark matter halos that host the galaxies we can also derive from them the cosmic bias, hence the effective halo masses associated to the tracer populations. Although the bias factors can also be well determined from the auto-power spectra, we must always beware of unaccounted systematic effects. The cross-correlation measurements are not prone to systematics that are not correlated between the two datasets. Thus a comparison of the bias estimates from auto- and cross-correlations can uncover unforeseen systematics on either side.

Several catalogs, such as those from the NRAO VLA Sky Survey (NVSS), the Sloan Digital Sky Survey (SDSS), the Wide Field Survey Infrared Explorer (WISE) have already been cross-correlated with the CMB lensing potential. These surveys cover large areas of the sky but detected sources are mostly at  $z \lesssim 1$ . The *Herschel* Terahertz Large Area survey (H-ATLAS; Eales et al. 2010) allows us to extend the cross-correlation analysis up to substantially higher redshifts (Lapi et al. 2011; González-Nuevo et al. 2012).

In this paper we present the first investigation of the cross-correlation between the CMB lensing potential measured by *Planck* and *Herschel*-selected galaxies with estimated redshifts  $z \gtrsim 1.5$ , i.e. at redshifts higher and closer to the peak of the lensing potential kernel than those of source samples considered so far. Our choice of restricting the analysis to  $z \gtrsim 1.5$  has a twofold motivation. First, since we aim at reconstructing the evolution of the lensing potential at higher redshifts than done with other galaxy samples, it is expedient to remove the dilution of the signal by low- $z$  sources. Second, as shown by Lapi et al. (2011) and González-Nuevo et al. (2012), the adopted approach for estimating photometric redshifts becomes unreliable at  $z \lesssim 1$ .

Highly statistically significant correlations between the CMB lensing and the Cosmic Infrared Background (CIB) have been recently reported (Holder et al. 2013; Hanson et al. 2013; Planck Collaboration XVIII 2013; POLARBEAR Collaboration 2014). There are obvious connections between these studies and the present one. However, the CIB is an integrated quantity and the interpretation of the measured cross-correlations depend on the adopted redshift distribution of sources, derived from a model. Our study of the cross-correlation with individually detected sources has the double advantage that redshifts are estimated directly from the data and are distributed over a quite narrow range.

The outline of this paper is as follows. In Section 2 we describe the theoretical background while the data are introduced in Section 3. The estimator of the cross-correlation power spectrum and the simulations used for validation of the algorithm and the error estimation are

presented in Section 4. The measured auto- and cross-power spectra, as well as the null tests, are reported in Section 5. In Section 6 we analyze the constraints on the galaxy bias and in Section 7 we discuss the potential systematic effects affecting the cross-correlation. Finally in Section 8 we summarize our results.

Throughout this paper we adopt the fiducial flat  $\Lambda$ CDM cosmology with best-fit *Planck* + WP + highL + lensing cosmological parameters as provided by the *Planck* team in Planck Collaboration XVI (2013). Here WP refers to WMAP polarization data at low multipoles, highL refers to the inclusion of high-resolution CMB data of the Atacama Cosmology Telescope (ACT) and South Pole Telescope (SPT) experiments and lensing refers to the inclusion of *Planck* CMB lensing data in the parameter likelihood.

## 2. THEORETICAL BACKGROUND

The effect of gravitational lensing on CMB photons can be described as a re-mapping of the unlensed temperature anisotropies  $\Theta(\hat{\mathbf{n}})$  by a two-dimensional vector field in the sky, namely the deflection field  $\mathbf{d}(\hat{\mathbf{n}})$  (Lewis & Challinor 2006):

$$\begin{aligned}\tilde{\Theta}(\hat{\mathbf{n}}) &= \Theta(\hat{\mathbf{n}} + \mathbf{d}(\hat{\mathbf{n}})) \\ &= \Theta(\hat{\mathbf{n}} + \nabla\phi(\hat{\mathbf{n}})) \\ &= \Theta(\hat{\mathbf{n}}) + \nabla^i\phi(\hat{\mathbf{n}})\nabla_i\Theta(\hat{\mathbf{n}}) + \mathcal{O}(\phi^2),\end{aligned}\quad (1)$$

where  $\tilde{\Theta}(\hat{\mathbf{n}})$  are the lensed temperature anisotropies and  $\phi(\hat{\mathbf{n}})$  is the CMB lensing potential:

$$\phi(\hat{\mathbf{n}}) = -2 \int_0^{z_*} \frac{cdz}{H(z)} \frac{\chi_* - \chi(z)}{\chi_*\chi(z)} \Psi(\chi(z)\hat{\mathbf{n}}, z). \quad (2)$$

In this equation,  $\chi(z)$  is the comoving distance to redshift  $z$ ,  $\chi_*$  is the comoving distance to the last scattering surface at  $z_* \simeq 1090$ ,  $H(z)$  is the Hubble factor at redshift  $z$ ,  $c$  is the speed of light, and  $\Psi(\chi(z)\hat{\mathbf{n}}, z)$  is the 3D gravitational potential at a point on the photon path given by  $\chi(z)\hat{\mathbf{n}}$ . Note that the deflection angle is given by  $\mathbf{d}(\hat{\mathbf{n}}) = \nabla\phi(\hat{\mathbf{n}})$ , where  $\nabla$  is the two-dimensional gradient on the sphere. Since the lensing potential is an integrated measure of the projected gravitational potential, taking the two-dimensional Laplacian of the lensing potential we can define the lensing convergence  $\kappa(\hat{\mathbf{n}}) = -\frac{1}{2}\nabla^2\phi(\hat{\mathbf{n}})$  which depends on the projected matter overdensity  $\delta$  (Bartelmann & Schneider 2001):

$$\kappa(\hat{\mathbf{n}}) = \int_0^{z_*} dz W^\kappa(z)\delta(\chi(z)\hat{\mathbf{n}}, z). \quad (3)$$

The lensing kernel  $W^\kappa$  is

$$W^\kappa(z) = \frac{3\Omega_m}{2c} \frac{H_0^2}{H(z)} (1+z)\chi(z) \frac{\chi_* - \chi(z)}{\chi_*}, \quad (4)$$

where  $\Omega_m$  and  $H_0$  are the present-day values of the Hubble and matter density parameters, respectively.

The galaxy overdensity  $g(\hat{\mathbf{n}})$  in a given direction on the sky is also expressed as a line-of-sight integral of the matter overdensity,

$$g(\hat{\mathbf{n}}) = \int_0^{z_*} dz W^g(z)\delta(\chi(z)\hat{\mathbf{n}}, z), \quad (5)$$

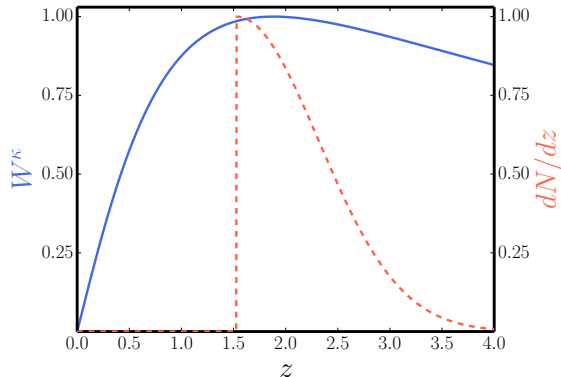


**Figure 1.** Estimated redshift distribution of the full sample of H-ATLAS galaxies (dashed red line) compared with the CMB lensing kernel  $W^\kappa$  (blue solid line). Both the kernels are normalized to a unit maximum.

where the kernel is

$$W^g(z) = \frac{b(z) \frac{dN}{dz}}{\left(\int dz' \frac{dN}{dz'}\right)} + \frac{3\Omega_m}{2c} \frac{H_0^2}{H(z)} (1+z)\chi(z) \times \int_z^{z_*} dz' \left(1 - \frac{\chi(z)}{\chi(z')}\right) (\alpha(z') - 1) \frac{dN}{dz'}. \quad (6)$$

The galaxy overdensity kernel is the sum of two terms: the first one is given by the product of the linear bias  $b(z)$  and the redshift distribution  $dN/dz$ ; and the second one takes into account the effect of gravitational magnification on the observed density of foreground sources (magnification bias; Ho et al. 2008; Xia et al. 2009). This effect depends on the slope,  $\alpha(z)$ , of their integral counts ( $N(> S) \propto S^{-\alpha}$ ) below the adopted flux density limit. Given the sharply peaked redshift distribution of our sources (see Fig. 1) we can safely assume a redshift- and scale-independent linear bias ( $b(z) = \text{constant}$ ). Previous analyses of the clustering properties of sub-mm galaxies (Xia et al. 2012; Cai et al. 2013) indicate  $b \simeq 3$  at the redshifts of interest here and we adopt this as our reference value.

Recent work by González-Nuevo et al. (2014) has shown that the magnification bias by weak lensing is substantial for high- $z$  H-ATLAS sources selected with the same criteria as the present sample (see the sub-section 3.2). This is because the source counts are steep, although their slope below the adopted flux density limit ( $S_{250\mu\text{m}} = 35 \text{ mJy}$ ) is uncertain. The data (Béthermin et al. 2012) indicate, at this limit,  $\alpha \simeq 2$  while for the high- $z$  galaxy sub-sample considered in this work we find  $\alpha \simeq 3$ . In the following we adopt the latter as our fiducial value. The effect of different choices for this parameter value is examined in Section 7.

Since the relevant angular scales are much smaller than 1 radian (multipoles  $\ell \gtrsim 100$ ) the theoretical angular cross-correlation can be computed using the Limber approximation (Limber 1953) as

$$C_\ell^{\kappa g} = \int_0^{z_*} \frac{dz}{c} \frac{H(z)}{\chi^2(z)} W^\kappa(z) W^g(z) P\left(k = \frac{\ell}{\chi(z)}, z\right), \quad (7)$$

where  $P(k, z)$  is the matter power spectrum, which we

computed using the CAMB<sup>14</sup> code (Lewis et al. 2000). The non-linear evolution of the matter power spectrum was taken into account using the HALOFIT prescription (Smith et al. 2003). A more extended discussion on the effect of the non-linear evolution in CMB lensing maps based on N-body simulations is carried out by Antolini et al. (2014). The CMB convergence,  $W^\kappa(z)$ , and the galaxy redshift distribution  $dN/dz$  of the sample analyzed in this work (see sub-section 3.2) are shown in Figure 1.

Again under the Limber approximation the CMB convergence,  $C_\ell^{\kappa\kappa}$ , and the galaxy,  $C_\ell^{gg}$ , auto-spectra can be evaluated as:

$$C_\ell^{\kappa\kappa} = \int_0^{z_*} \frac{dz}{c} \frac{H(z)}{\chi^2(z)} [W^\kappa(z)]^2 P\left(k = \frac{\ell}{\chi(z)}, z\right); \quad (8)$$

$$C_\ell^{gg} = \int_0^{z_*} \frac{dz}{c} \frac{H(z)}{\chi^2(z)} [W^g(z)]^2 P\left(k = \frac{\ell}{\chi(z)}, z\right).$$

The mean redshift probed by the cross-correlation between CMB lensing and our sample is

$$\langle z \rangle = \frac{\int_0^{z_*} \frac{dz}{c} z \frac{H(z)}{\chi^2(z)} W^\kappa(z) W^g(z) P\left(k = \frac{\ell}{\chi(z)}, z\right)}{\int_0^{z_*} \frac{dz}{c} \frac{H(z)}{\chi^2(z)} W^\kappa(z) W^g(z) P\left(k = \frac{\ell}{\chi(z)}, z\right)} \simeq 2. \quad (9)$$

We can predict the signal to noise ratio (S/N) of the convergence-density correlation assuming that both the galaxy overdensity and the lensing fields behave as Gaussian random fields, so that the variance of  $C_\ell^{\kappa g}$  is

$$(\Delta C_\ell^{\kappa g})^2 = \frac{1}{(2\ell + 1) f_{\text{sky}}} [(C_\ell^{\kappa g})^2 + (C_\ell^{\kappa\kappa} + N_\ell^{\kappa\kappa})(C_\ell^{gg} + N_\ell^{gg})], \quad (10)$$

where  $f_{\text{sky}}$  is the sky fraction covered by both the galaxy and the lensing surveys,  $N_\ell^{\kappa\kappa}$  is the noise of the lensing field, and  $N_\ell^{gg} = 1/\bar{n}$  is the shot noise associated with the galaxy field. Since our calculations are done in terms of the density contrast the shot noise is inversely proportional to the mean number of sources per steradian,  $\bar{n}$ . The signal to noise ratio at multipole  $\ell$  is then

$$\left(\frac{S}{N}\right)_\ell = \frac{(C_\ell^{\kappa g})^2}{(\Delta C_\ell^{\kappa g})^2} = \frac{(2\ell + 1) f_{\text{sky}} (C_\ell^{\kappa g})^2}{[(C_\ell^{\kappa g})^2 + (C_\ell^{\kappa\kappa} + N_\ell^{\kappa\kappa})(C_\ell^{gg} + N_\ell^{gg})]}, \quad (11)$$

and the cumulative signal to noise ratio for multipoles up to  $\ell_{\text{max}}$  is

$$\left(\frac{S}{N}\right)(< \ell_{\text{max}}) = \sqrt{\sum_{\ell'=\ell_{\text{min}}}^{\ell_{\text{max}}} \left(\frac{S}{N}\right)_{\ell'}^2}. \quad (12)$$

In Figure 2 we show both the signal to noise per multipole and the cumulative one computed using the specifications for the *Planck* lensing noise (see sub-section 3.1) and the mean surface density of our source sample. It must be noted that, due to the limited area covered by the H-ATLAS survey (and split into 5 fields) the cross-correlation is only meaningful on scales below a few degrees. We have therefore limited our analysis to  $\ell \geq \ell_{\text{min}} = 100$ . This restriction prevents us from exploiting the peak at  $\ell \sim 100$  of the signal to noise per

<sup>14</sup> available at <http://camb.info>

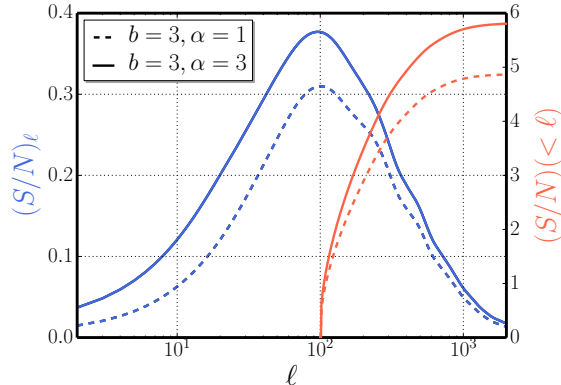


**Figure 2.** Signal to noise ratio per multipole (blue lines; left axis) and cumulative signal to noise ratio (red lines; right axis) evaluated from  $\ell_{\min} = 100$  for fiducial models with  $b = 3$  and  $\alpha = 1$  (no magnification, dashed lines) and  $\alpha = 3$  (solid lines).

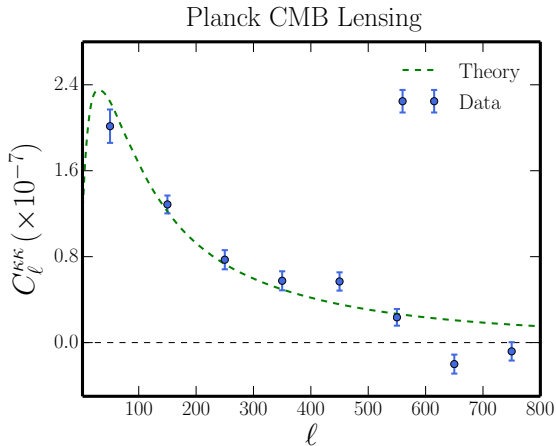


**Figure 3.** CMB convergence auto-power spectrum as reconstructed from *Planck* data (blue points) on a portion of the sky with  $f_{\text{sky}} \simeq 0.6$  compared with the theoretical prediction for our background cosmology (dashed green line).

multipole. The cumulative signal to noise ratio saturates at  $\ell \sim 1000$ . If  $b = 3$  and  $\alpha = 3$  we expect  $S/N \simeq 6$ .

### 3. DATA

#### 3.1. Planck data

We used the publicly released *Planck* CMB lensing potential map derived from the first 15.5 months of observations (Planck Collaboration XVII 2013). The *Planck* satellite observed the sky with high angular resolution in nine frequency bands, from 30 to 857 GHz (Planck Collaboration I 2013). The angular resolution ( $10'$ ,  $7'$  and  $5'$ ) and the noise level (105, 45 and  $60 \mu\text{K arcmin}$ ) of the 100, 143 and 217 GHz frequency channels, respectively, make them the most suitable for estimation of the gravitational lensing potential. Nevertheless, the released map is based on a minimum variance combination of the 143 and 217 GHz temperature anisotropy maps only, as adding the 100 GHz map yields a negligible improvement (Planck Collaboration XVII 2013). The maps are in the HEALPIX<sup>15</sup> (Górski et al. 2005) format with a resolution parameter  $N_{\text{side}} = 2048$ , corresponding to 50

<sup>15</sup> <http://healpix.jpl.nasa.gov>

331 648 pixels over the sky, with a pixel size of  $\sim 1.7'$ .

The power spectrum of the lensing potential is very red and this may introduce a bias when we estimate it within multipole bins. To avoid this problem we decided to convert the lensing potential map,  $\phi$ , into the convergence map,  $\kappa$ , which has a much less red power spectrum. This was done using the relation between the spherical harmonic coefficients of these quantities estimated on the full sky (Hu 2000)

$$\kappa_{\ell m} = -\frac{\ell(\ell+1)}{2}\phi_{\ell m}. \quad (13)$$

The convergence spherical harmonic coefficients were transformed to a map with resolution parameter  $N_{\text{side}} = 512$  corresponding to a pixel size of  $\sim 7'$ . This resolution is sufficient for our analysis because the data noise level enables us to detect cross-correlations between the convergence and the galaxy density field only for angular scales larger than  $\sim 20'$  ( $\ell \lesssim 540$ ).

The convergence auto-power spectrum recovered on approximately 60% of the sky using a modified version of the mask provided by the *Planck* collaboration is shown in Fig. 3. The auto-power spectrum has been corrected for the lensing reconstruction noise power spectrum  $N_\ell^{\kappa\kappa}$  which was estimated from the set of 100 simulated lensing maps<sup>16</sup> recently released by *Planck* team that account for the inhomogeneous noise level. The noise power spectrum was computed by averaging spectra of difference maps between the reconstructed and the input lensing map over 100 realizations. The errors on bandpowers were calculated as the diagonal part of the covariance matrix built from the simulation as described in Sec. 4. The raw auto-power spectrum is not corrected for the bias induced by non-Gaussianity of unresolved point sources and for pseudo- $C_\ell$  leakage effects from masking (we just correct for N0 and N1 bias term adopting the formalism of Planck Collaboration XVII (2013)). These terms may cause some discrepancy of the power spectrum at high multipoles, nevertheless, in the range of multipoles relevant for our analysis the power spectrum agrees pretty well with the theoretical one and proper estimation of the convergence power spectrum is out of scope of this paper.

#### 3.2. Herschel fields

We exploited the data collected by the *Herschel* Space Observatory (Pilbratt et al. 2010) in the context of the *Herschel* Astrophysical Terahertz Large Area Survey (H-ATLAS; Eales et al. 2010), an open-time key program that has surveyed about  $550 \text{ deg}^2$  with the Photodetector Array Camera and Spectrometer (PACS; Poglitsch et al. 2010) and the Spectral and Photometric Imaging Receiver (SPIRE; Griffin et al. 2010) in five bands, from 100 to  $500 \mu\text{m}$ . The H-ATLAS map-making is described by Pascale et al. (2011) for SPIRE and by Ibar et al. (2010) for PACS. The procedures for source extraction and catalogue generation can be found in Rigby et al. (2011), Maddox *et al.* (in preparation) and Valiante *et al.* (in preparation).

The survey area is divided into five fields: three equatorial fields centered on 9hr, 12hr and 14.5hr (GAMA fields,

<sup>16</sup> [http://irsa.ipac.caltech.edu/data/Planck/release\\_1/ancillary-data/HFI\\_Products.html](http://irsa.ipac.caltech.edu/data/Planck/release_1/ancillary-data/HFI_Products.html)

**Table 1**  
H-ATLAS patches data.

Patch	$N_{\text{obj}}$	$f_{\text{sky}}$	$\bar{n}$ [gal pix $^{-1}$ ]	$\bar{n}$ [gal sr $^{-1}$ ]
ALL	99823	0.014	2.30	$5.76 \times 10^5$
NGP	28245	0.004	2.25	$5.64 \times 10^5$
SGP	44449	0.006	2.38	$5.95 \times 10^5$
G09	9099	0.001	2.28	$5.71 \times 10^5$
G12	8751	0.001	2.13	$5.35 \times 10^5$
G15	9279	0.001	2.27	$5.68 \times 10^5$

<sup>a</sup> ALL is the combination of all the patches together

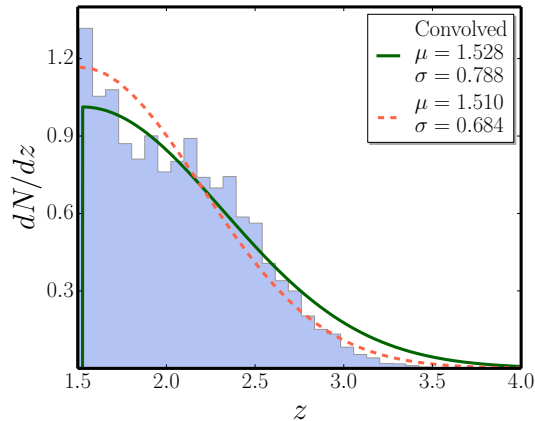


**Figure 4.** Redshift distribution of H-ATLAS galaxies for the combined set of patches used in the analysis. The (blue) histogram is the empirical redshift distributions, the dashed (orange) line is the half-normal fit to  $dN/dz$  as described in text, while the solid (green) line represents the convolved  $dN/dz$  that takes into account errors on photo- $z$  estimation and is used as the fiducial distribution in our analysis. The values of the parameters  $\mu$  and  $\sigma$  given in the box are the best-fit values and are used in the analytic expression for  $dN/dz$  adopted in calculations.

G09, G12 and G15) covering, altogether, 161 deg $^2$ ; the North Galactic Pole (NGP) block, a rectangular block of 15 $^\circ$   $\cos(\delta)$  by 10 $^\circ$  centered on right ascension  $\alpha = 199.5^\circ$ , declination  $\delta = 29^\circ$  and rotated by approximately 8 $^\circ$  clockwise; and the South Galactic Pole (SGP) block consisting of two concatenated rectangular regions, one of 31.5 $^\circ$   $\cos(\delta)$  by 6 $^\circ$  centered on  $\alpha = 351.3^\circ$ ,  $\delta = -32.8^\circ$ , the other of 20 $^\circ$   $\cos(\delta)$  by 6 $^\circ$  centered on  $\alpha = 18.1^\circ$ ,  $\delta = -30.7^\circ$ .

The  $z \lesssim 1$  galaxies detected by the H-ATLAS survey are mostly late-type and starburst galaxies with moderate star formation rates and relatively weak clustering (Dunne et al. 2011; Guo et al. 2011). High- $z$  galaxies are forming stars at high rates ( $\geq$  few hundred  $M_\odot \text{ yr}^{-1}$ ) and are much more strongly clustered (Maddox et al. 2010; Xia et al. 2012), implying that they are tracers of large scale over-densities. Their properties are consistent with them being the progenitors of local massive elliptical galaxies (Lapi et al. 2011). We aim at correlating high- $z$  H-ATLAS galaxies with the *Planck* CMB lensing map.

To select the high- $z$  population we adopted the criteria developed by González-Nuevo et al. (2012): (i)  $S_{250 \mu\text{m}} > 35$  mJy; (ii)  $S_{350 \mu\text{m}}/S_{250 \mu\text{m}} > 0.6$  and  $S_{500 \mu\text{m}}/S_{350 \mu\text{m}} > 0.4$ ; (iii)  $3\sigma$  detection at 350  $\mu\text{m}$ ; and (iv) photometric redshift  $z_{\text{phot}} > 1.5$ , estimated following

Lapi et al. (2011) and González-Nuevo et al. (2012).

Our final sample comprises a total of 99 823 sources, of which 9099 are in G09, 8751 in G12, 9279 in G15, 28245 in NGP and 44449 in SGP. The specifics of each patch are summarized in Table 1. The redshift distribution of the population is needed in order to predict the amplitude of the cross-correlation. Estimating the uncertainties in the redshift distribution due to photometric redshift errors is not a trivial task.

As stated in González-Nuevo et al. (2012) there is no indication that photometric redshifts are systematically under- or overestimated when the SED of SMM J2135-0102 is used as a template. The median value of  $\Delta z/(1+z) \equiv (z_{\text{phot}} - z_{\text{spec}})/(1+z_{\text{spec}})$  is -0.002 with a dispersion of 0.115. This dispersion corresponds to an rms error on  $z$ ,  $\sigma_{(z)} = 0.345$  at the mean redshift  $\langle z \rangle \simeq 2$ , given by eq. (9). To get a rough indication of how many sources were scattered above and below the redshift threshold ( $z = 1.5$ ) by measurement errors we have convolved a gaussian fit to the redshift distribution of sources selected with the first 3 criteria [(i) to (iii)] with a gaussian error distribution having zero mean and dispersion  $\sigma_{(z)}$ . The convolved redshift distribution was cut at  $z = 1.5$  and the portion at higher  $z$  was fitted with a half-normal distribution normalized to unity:

$$\frac{dN}{dz} = \frac{\sqrt{2}}{\sigma\sqrt{\pi}} \exp\left(-\frac{(z-\mu)^2}{2\sigma^2}\right). \quad (14)$$

The redshift distributions of the galaxies before and after the convolution are shown in Fig. 4.

We built an overdensity map at a resolution  $N_{\text{side}} = 512$  defined by

$$g(\hat{\mathbf{n}}) = \frac{n(\hat{\mathbf{n}}) - \bar{n}}{\bar{n}}, \quad (15)$$

where  $n(\hat{\mathbf{n}})$  is the number of objects in a given pixel, and  $\bar{n}$  is the mean number of objects per pixel. The CMB convergence and galaxy overdensity maps in the different patches are shown in Fig. 5. We filtered out from these fields multipoles  $\ell \gtrsim 400$  where  $(S/N)_\ell \lesssim 0.3$ .

## 4. THE CROSS-CORRELATION ALGORITHM

### 4.1. Estimator

We computed the angular power spectra within the regions covered by the H-ATLAS survey using a pseudo- $C_\ell$  estimator based on the MASTER algorithm (Hivon et al. 2002). These regions are inside the area used in the estimation of the CMB lensing map. For a survey that covers only a fraction of the sky different modes of the true cross-power spectrum  $C_\ell^{\kappa g}$  are coupled (Hauser & Peebles 1973). The coupling can be described by the mode-mode coupling matrix  $M_{\ell\ell'}$  which relates the pseudo cross-spectrum  $\tilde{C}_\ell^{\kappa g}$  measured from the data:

$$\tilde{C}_\ell^{\kappa g} = \frac{1}{2\ell+1} \sum_{m=-\ell}^{\ell} \tilde{\kappa}_{\ell m} \tilde{g}_{\ell m}^*. \quad (16)$$

to the true power spectrum:

$$\tilde{C}_\ell^{\kappa g} = \sum_{\ell'} M_{\ell\ell'} C_{\ell'}^{\kappa g}. \quad (17)$$

However we cannot directly invert eq. (17) to get the true power spectrum, because for surveys covering only

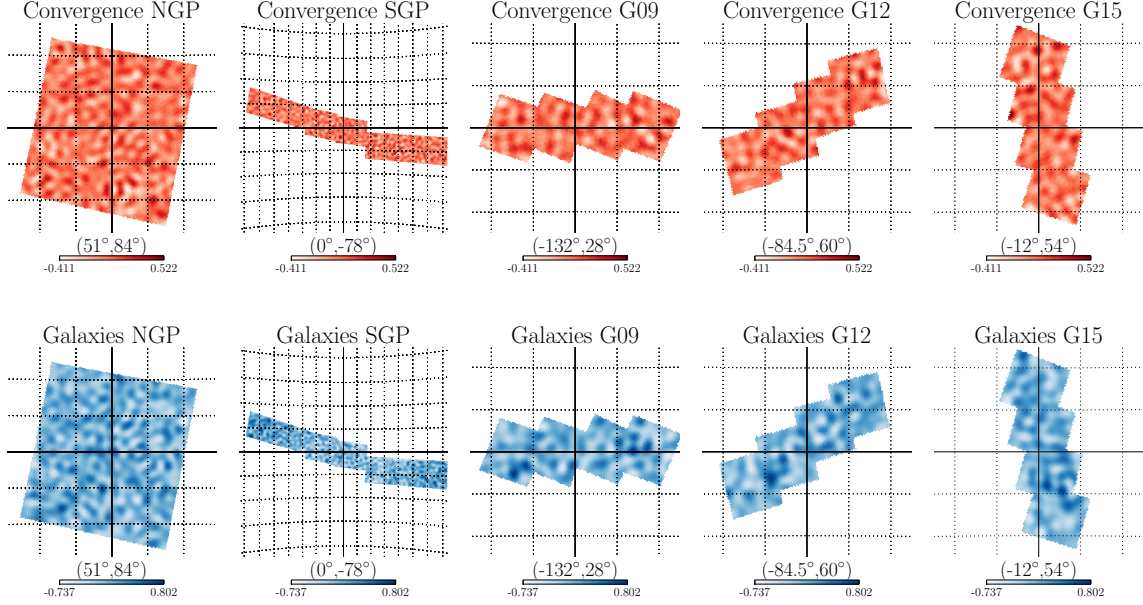


**Figure 5.** Convergence maps (upper row) and galaxy overdensity maps (lower row) in the H-ATLAS fields: multipoles  $\ell > 400$  for which  $(S/N)_\ell \lesssim 0.3$  have been filtered out. Galactic longitude and latitude ( $l, b$ ) of patches centers are provided in brackets. The grid overlay has spacing of  $3^\circ$  in each box.

a small fraction of the sky the coupling matrix  $M_{\ell\ell'}$  becomes singular. To reduce the correlations of the  $C_\ell$ 's it is necessary to bin the power spectrum in  $\ell$ . We used eight linearly spaced bins of width  $\Delta\ell = 100$  in the range  $0 \leq \ell \leq 800$ .

Then, the estimator of the true bandpowers  $\hat{C}_L^{\kappa g}$  (hereafter  $C_L^{\kappa g}$  denotes the binned power spectrum and  $L$  identifies the bin) is given by

$$\hat{C}_L^{\kappa g} = \sum_{L'\ell} K_{LL'}^{-1} P_{L'\ell} \tilde{C}_\ell^{\kappa g}, \quad (18)$$

where

$$K_{LL'} = \sum_{\ell\ell'} P_{L\ell} M_{\ell\ell'} B_{\ell'}^2 Q_{\ell'L'}. \quad (19)$$

Here  $P_{L\ell}$  is the binning operator,  $Q_{\ell L}$  and  $B_{\ell'}^2$  are, respectively, the reciprocal of the binning operator and the pixel window function that takes into account the finite pixel size. Because of the small size of the sky area covered by the H-ATLAS survey the power spectrum for  $\ell < 100$  is very poorly estimated, and we did not use it in our analysis. However, to avoid the bias coming from the lowest order multipoles, the first multipole bin is included in the computation of the power spectrum, i.e. the inversion of the binned coupling matrix  $K_{LL'}$  is performed including the first bin and the pseudo-power spectrum for the first bin is used in the product of eq. (18).

The main assumption in cross-correlation studies is that the noise levels related to the observables being analyzed are uncorrelated so that we do not need to de-bias the reconstructed cross-spectrum for any noise term. However, when dealing with auto-power spectra, such as  $C_\ell^{gg}$  and  $C_\ell^{\kappa\kappa}$ , we have to correct the estimator given by

eq. (18) in order to account for the noise

$$\begin{aligned} \hat{C}_L^{gg} &= \sum_{L'\ell} K_{LL'}^{-1} P_{L'\ell} \left( \tilde{C}_\ell^{gg} - \langle \tilde{N}_\ell^{gg} \rangle_{\text{MC}} \right), \\ \hat{C}_L^{\kappa\kappa} &= \sum_{L'\ell} K_{LL'}^{-1} P_{L'\ell} \left( \tilde{C}_\ell^{\kappa\kappa} - \langle \tilde{N}_\ell^{\kappa\kappa} \rangle_{\text{MC}} \right), \end{aligned} \quad (20)$$

where  $\langle \tilde{N}_\ell^{gg} \rangle_{\text{MC}}$  and  $\langle \tilde{N}_\ell^{\kappa\kappa} \rangle_{\text{MC}}$  are the average noise pseudo-spectra estimated from the Monte Carlo (MC) simulations.

#### 4.2. Covariance matrix

The errors on the cross-power spectrum are described by the covariance matrix (Brown et al. 2005)

$$\text{Cov}_{LL'}^{\kappa g} = M_{LL'}^{-1} P_{L_1\ell} \widetilde{\text{Cov}}_{\ell\ell'}^{\kappa g} Q_{\ell'L_2} (M_{L'L_2}^{-1})^T, \quad (21)$$

where  $\widetilde{\text{Cov}}_{\ell\ell'}^{\kappa g}$  is the pseudo-covariance matrix given by

$$\begin{aligned} \widetilde{\text{Cov}}_{\ell\ell'}^{\kappa g} &= \frac{1}{2\ell' + 1} M_{\ell\ell'} \left[ C_\ell^{\kappa g}(b) C_{\ell'}^{\kappa g}(b) + \right. \\ &\quad \left. \sqrt{(C_\ell^{\kappa\kappa} + N_\ell^{\kappa\kappa})(C_\ell^{gg}(b) + N_\ell^{gg})(C_{\ell'}^{\kappa\kappa} + N_{\ell'}^{\kappa\kappa})(C_{\ell'}^{gg}(b) + N_{\ell'}^{gg})} \right]. \end{aligned} \quad (22)$$

The corresponding covariance matrix of the galaxy auto-correlation is obtained by replacing in eq. (21) the pseudo-covariance matrix  $\widetilde{\text{Cov}}_{\ell\ell'}^{\kappa g}$  with  $\widetilde{\text{Cov}}_{\ell\ell'}^{gg}$  given by

$$\widetilde{\text{Cov}}_{\ell\ell'}^{gg} = \frac{2}{2\ell' + 1} M_{\ell\ell'} \left[ (C_\ell^{gg}(b) + N_\ell^{gg})(C_{\ell'}^{gg}(b) + N_{\ell'}^{gg}) \right]. \quad (23)$$

The analytical expressions for the covariance matrices given above were used in the estimation of the galaxy bias and of the amplitude of the cross-correlation, presented in Section 6.

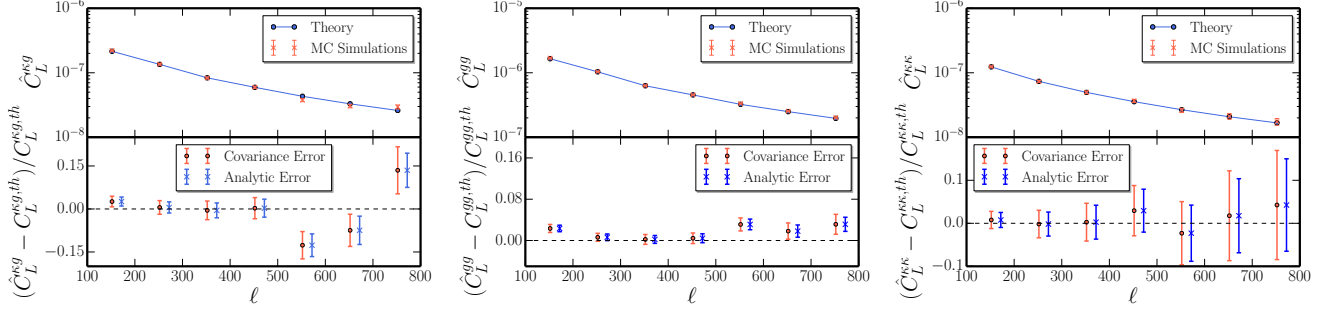


**Figure 6.** *Left. Upper panel:* Cross-power spectrum of simulated galaxy and lensing maps constructed with  $b = 3$ . The points connected by the solid blue line represent the binned input cross-spectrum while the average reconstructed spectrum from 500 simulations is shown by the orange points. *Lower panel:* Fractional difference between the input and extracted cross-spectra. Error bars obtained with the simulation covariance matrix (orange points) and with the analytical approximation (blue points) are shown for comparison. *Middle.* As in left plot, but for the galaxy auto-power spectrum. *Right.* As in left plot, but for the CMB convergence auto-power spectrum

### 4.3. Validation

In order to validate the algorithms used for the computation of the estimators outlined in the previous section and to check that the cross- and auto-power spectra estimates are unbiased, we created 500 simulated maps of the CMB convergence field and of the galaxy overdensity field with statistical properties consistent with observations.

Using the theoretical spectra obtained with eqs. (7) and (8), we generated full sky signal maps injecting a known degree of correlation, so that the simulated CMB convergence and galaxy harmonic modes satisfy both the auto- and the cross-correlations (Kamionkowski et al. 1997):

$$\begin{aligned} \kappa_{\ell m} &= \zeta_1 (C_{\ell}^{\kappa\kappa})^{1/2}; \\ g_{\ell m} &= \zeta_1 \frac{C_{\ell}^{\kappa g}}{(C_{\ell}^{\kappa\kappa})^{1/2}} + \zeta_2 \left[ C_{\ell}^{gg} - \frac{(C_{\ell}^{\kappa g})^2}{C_{\ell}^{\kappa\kappa}} \right]^{1/2}. \end{aligned} \quad (24)$$

For each value of  $\ell$  and  $m > 0$ ,  $\zeta_1$  and  $\zeta_2$  are two complex numbers drawn from a Gaussian distribution with unit variance, while for  $m = 0$  they are real and normally distributed.

We also generated 500 noise realizations for both fields. To simulate Gaussian convergence noise maps we used the convergence noise power spectrum  $N_{\ell}^{\kappa\kappa}$  provided by the *Planck* team<sup>17</sup>. Although this power spectrum is not sufficiently accurate for the estimation of the convergence power spectrum, as pointed out in the *Planck* Collaboration Products website, it should be sufficiently good for the cross-correlation analysis which is not biased by the noise term. For the same reason it is not crucial for our analysis to use the 100 simulations of the estimated lensing maps provided recently by the *Planck* team.

To take into account noise in the simulated galaxy maps, we proceeded in the following way. For each signal map containing the galaxy overdensity, we generated a set of simulated galaxy number count maps, where the value in each pixel is drawn from a Poisson distribution with mean

$$\lambda(\hat{\mathbf{n}}) = \bar{n}(1 + g(\hat{\mathbf{n}})), \quad (25)$$

where  $\bar{n}$  is the mean number of sources per pixel in a given H-ATLAS patch and  $g(\hat{\mathbf{n}})$  is the correspond-

ing simulated galaxy map containing only signal. The galaxy number counts map  $\lambda(\hat{\mathbf{n}})$  was then converted into a galaxy overdensity map using eq. (15), substituting the real number of objects in a given pixel  $n(\hat{\mathbf{n}})$  with the simulated one  $\lambda(\hat{\mathbf{n}})$ . Note that maps obtained in this way already include Poisson noise with variance  $N_{\ell}^{gg} = 1/\bar{n}$ .

We applied the pipeline described above to our set of simulations in order to recover the input cross- and auto-power spectra used to generate such simulations. The extracted  $\hat{C}_L^{\kappa g}$ ,  $\hat{C}_L^{gg}$ , and  $\hat{C}_L^{\kappa\kappa}$  spectra averaged over 500 simulations are reported in Fig. 6. The mean band-power was computed as:

$$\langle \hat{C}_L^{XY} \rangle = \frac{1}{N_{\text{sim}}} \sum_{i=1}^{N_{\text{sim}}} \hat{C}_L^{XY,i}, \quad (26)$$

where  $X, Y = \{\kappa, g\}$ ,  $i$  refers to the  $i$ -th simulation, and  $N_{\text{sim}} = 500$  is the number of simulations. The errors were computed from the covariance matrix as

$$\Delta \hat{C}_L^{XY} = \left( \frac{\text{Cov}_{LL}^{XY}}{N_{\text{sim}}} \right)^{1/2}, \quad (27)$$

and the covariance matrix  $\text{Cov}_{LL'}^{XY}$  was evaluated from the simulations as

$$\text{Cov}_{LL'}^{XY} = \frac{1}{N_{\text{sim}} - 1} \sum_{i=1}^{N_{\text{sim}}} (\hat{C}_L^{XY,i} - \langle \hat{C}_L^{XY} \rangle) (\hat{C}_{L'}^{XY,i} - \langle \hat{C}_{L'}^{XY} \rangle). \quad (28)$$

We also show, for comparison, the theoretical error bars obtained from eq. (10), modified to take into account the binning. They are in generally good agreement with the Monte Carlo error estimates, which, however, are slightly larger (by up to  $\sim 25\%$ ).

## 5. POWER SPECTRA

### 5.1. CMB Convergence-Galaxy Cross-correlation

The recovered cross-spectrum is shown in Fig. 7. To compute it we have applied to both maps masks that select the five H-ATLAS patches of interest. The error bars are estimated cross-correlating 500 Monte Carlo realizations of simulated CMB convergence maps (consisting of both signal and noise) with the true H-ATLAS galaxy density map, as described in sub-section 5.3. This method assumes that the two maps are uncorrelated; our error estimates are a good approximation, since both maps are very noisy and  $C_{\ell}^{\kappa\kappa, \text{tot}} C_{\ell}^{gg, \text{tot}} \gg (C_{\ell}^{\kappa g})^2$ . We

<sup>17</sup> [http://wiki.cosmos.esa.int/planckpla/index.php/Specially\\_processed\\_maps](http://wiki.cosmos.esa.int/planckpla/index.php/Specially_processed_maps)

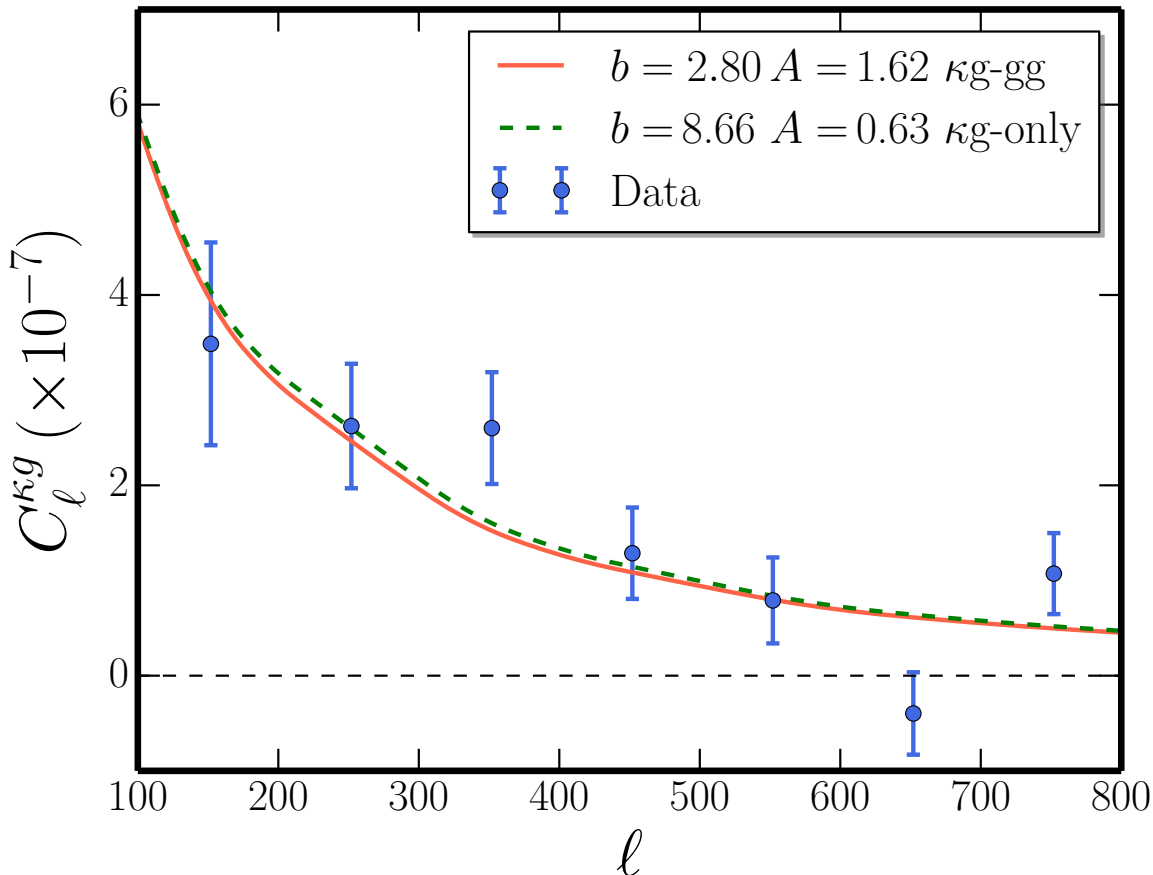


**Figure 7.** The CMB convergence - galaxy density cross-spectrum as measured from *Planck* and *Herschel* data. The data points are shown in blue, with error bars computed using the full covariance matrix obtained from Monte Carlo realizations of convergence maps. The theoretical spectra calculated with the bias values inferred from the likelihood analysis (as described in text) using the cross-correlation data only (solid red line) and the cross-correlation together with the galaxy auto-correlation data (dot-dashed green line) are also shown; we fix  $\alpha = 3$  in this analysis. The null (no correlation) hypothesis is rejected at the  $20\sigma$  level.

have also estimated the errors from cross-correlations of 500 Monte Carlo realizations of simulated H-ATLAS galaxy density maps with the real *Planck* CMB convergence map. The former approach yields slightly smaller error bars, yet slightly larger than those estimated analytically (see Fig. 8). These error estimates were checked by cross-correlating the publicly available set of 100 simulated lensing maps, that accurately reflect the *Planck* noise properties, with the real H-ATLAS map. The derived error bars are comparable with those found with our baseline approach and there is no sign of systematic under- or over-estimation.

We have exploited the simulations to build the covariance matrix, used to evaluate the probability that the measured signal is consistent with no correlation (our null hypothesis). As can be seen in Fig. 9, the covariance matrix is dominated by the diagonal components; however, off-diagonal components are non-negligible and have to be taken into account. The  $\chi^2$  was calculated as:

$$\chi_{\text{null}}^2 = \hat{\mathbf{C}}_L^{\text{kg}} (\text{Cov}_{LL'}^{\text{kg}})^{-1} \hat{\mathbf{C}}_{L'}^{\text{kg}}. \quad (29)$$

For the analysis performed with the whole H-ATLAS sample we obtained  $\chi_{\text{null}}^2 = 83.3$  for  $\nu = 7$  degrees of freedom, corresponding to a probability that the null hypothesis holds of  $p = 2.89 \times 10^{-15}$ . Since the  $\chi^2$  distribution has mean  $\nu$  and variance  $2\nu$ , the null hypothesis is

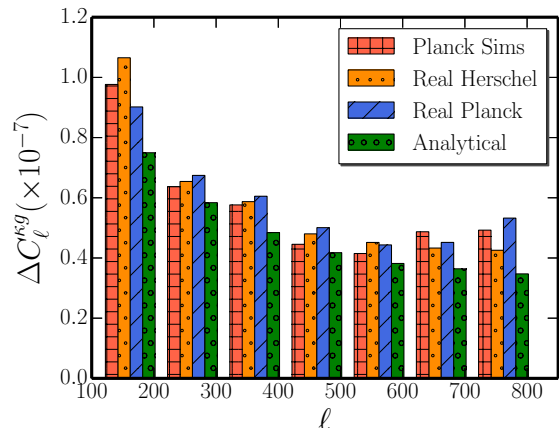


**Figure 8.** Error estimates for the cross-power spectrum bandpowers. The Monte Carlo estimates associated to estimated bandpowers are shown in orange (500 simulated lensing maps correlated with the real galaxy field). Blue bars represent errors obtained correlating 500 simulated galaxy maps with the real convergence field, while the green bars represent the analytical approximation to these errors. Errors estimates obtained correlating the real galaxy field with the 100 lensing simulated maps by the *Planck* collaboration are shown in red.

rejected with a significance of about  $(83.3 - 7)/(14^{1/2}) \simeq 20\sigma$ . This is the sum in quadrature of the significance of the correlation in each band-power, taking into account



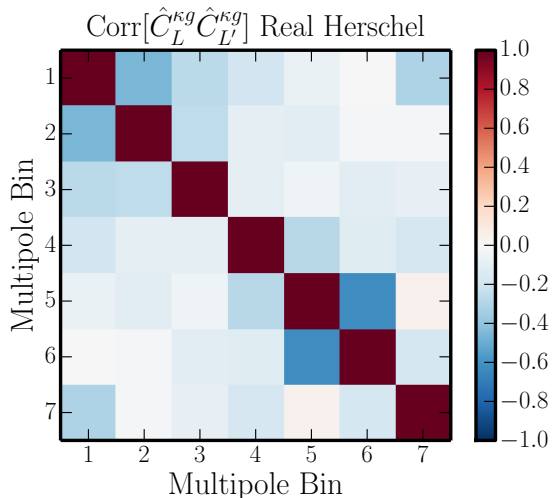


**Figure 9.** Correlation matrix  $\text{Corr}[\hat{C}_L^{\kappa g} \hat{C}_{L'}^{\kappa g}]$  built from the covariance matrix obtained by correlating 500 simulated lensing maps with the real H-ATLAS galaxy map.

**Table 2**  
Significance of no cross-correlation hypothesis rejection.

Patch	$\chi^2_{\text{null}}/\nu$	p-value	Significance
ALL	83.31/7	$2.89 \times 10^{-15}$	$20.3\sigma$
NGP	34.03/7	$1.70 \times 10^{-5}$	$7.2\sigma$
SGP	27.77/7	0.002	$5.6\sigma$
G09	22.41/7	0.002	$4.1\sigma$
G12	22.26/7	0.002	$4.1\sigma$
G15	29.23/7	$1.0 \times 10^{-4}$	$5.9\sigma$

the correlations between different bins. The results of the  $\chi^2$  analysis for each patch are reported in Table 2.

### 5.2. Galaxy Auto-correlation

We also performed an analysis of the auto-correlation of *Herschel* galaxies on the different patches. The shot noise subtracted auto-power spectrum measured for the complete H-ATLAS data set is shown in Figure 10. The error bars on the data points are evaluated from the diagonal part of the covariance matrix built from galaxy simulations with bias  $b = 3$ . The detected signal is highly significant ( $40\sigma$ ).

### 5.3. Null Tests

In order to verify our pipeline and the reconstructed spectra against the possibility of residual systematic errors we performed a series of null tests which consist in cross-correlating the real map of one field with simulated maps of the other field. Since there is no common cosmological signal, the mean correlation must be zero.

We cross-correlated our 500 simulated CMB lensing maps (containing both signal and noise) with the real H-ATLAS galaxy density contrast map and our 500 simulated galaxy maps constructed using  $b = 3$  with the true *Planck* CMB convergence map. The error bars on the cross-power spectra were computed using the covariance matrices obtained from these simulations. As illustrated in Figure 11 in both cases no significant signal was detected. In the first test we obtained  $\chi^2 = 7.2$  cor-

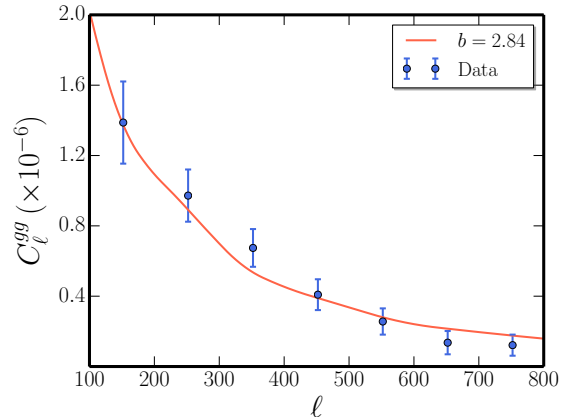


**Figure 10.** Galaxy density auto-power spectrum for the whole sample of H-ATLAS galaxies. The data points are shown in blue, while the solid (red) line is the theoretical  $C_\ell^{gg}$  evaluated for the best-fit value of the bias obtained using a likelihood analysis on the galaxy auto-spectrum data.

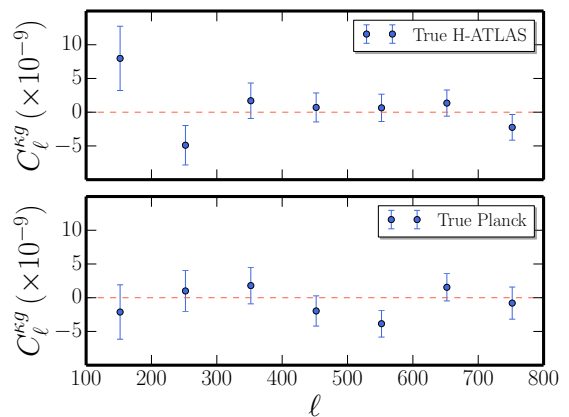


**Figure 11.** Results of null tests. *Upper panel:* mean correlation between the true H-ATLAS map including all the five patches and 500 simulated CMB lensing maps. *Lower panel:* mean cross-spectra between the true *Planck* lensing map and 500 simulated galaxy maps with  $b = 3$ . No significant signal is detected in either case.

responding to a probability of the null hypothesis (no correlation)  $p = 0.41$ , while in the second one we have  $\chi^2 = 5.9$  and  $p = 0.55$ .

A further test consisted in cross-correlating the galaxy distribution in one patch of the sky with the lensing map in another. We moved in turn the three H-ATLAS GAMA fields and the SGP field to the position of the NGP patch and shifted the NGP galaxies to the SGP area. Then we cross-correlated each shifted galaxy map with the convergence field in the same position. The errors on the cross-correlations were obtained as above. All of the cross-spectra are consistent with no signal.

## 6. CONSTRAINTS ON BIAS AND AMPLITUDE OF CROSS-CORRELATION

We now discuss the cross-correlation signal of cosmological origin. Following Planck Collaboration XVII (2013) we introduce an additional parameter,  $A$ , that scales the expected amplitude of the cross-power spectrum,  $C_\ell^{\kappa g}$ , of the *Planck* CMB lensing with the H-ATLAS galaxy overdensity map as  $A C_L^{\kappa g}(b)$ . Obviously, its expected value is 1. Because the theoretical cross-

spectrum is also basically proportional to the galaxy bias, there is strong degeneracy between these two parameters. In order to break this degeneracy we use also the galaxy auto-power spectrum which depends only on  $b$ .

The best-fit values of the amplitude and of the galaxy bias were obtained using the maximum likelihood approach. In the following we first describe the likelihood functions and present constraints on the redshift-independent galaxy bias and on the cross-correlation amplitude using galaxy auto-correlation data alone, cross-correlation data alone, and combining both datasets. In this analysis the cosmological parameters and the counts slope  $\alpha$  are kept fixed to the fiducial values. In order to efficiently sample the parameter space, we use the Markov Chain Monte Carlo (MCMC) method assuming uninformative flat priors. For this purpose we employ EMCEE (Foreman-Mackey et al. 2013), a public implementation of the affine invariant MCMC ensemble sampler (Goodman & Weare 2010). In this paper each quoted parameter estimate is the median of the appropriate posterior distribution after marginalizing over the remaining parameters with uncertainties given by the 16<sup>th</sup> and 84<sup>th</sup> percentiles (indicating the bounds of a 68% credible interval). For a Gaussian distributions, as is the case when combining both datasets, these percentiles correspond approximately to  $-1\sigma$  and  $+1\sigma$  values and the median of the posterior is equal to the mean and maximum likelihood value.

We assumed Gaussian likelihood functions for the cross- and auto-power spectra. For the galaxy auto-power spectrum it takes the form

$$\mathcal{L}(\hat{C}_L^{gg}|b) = \frac{1}{\sqrt{(2\pi)^{N_L} \det(\text{Cov}_{LL'}^{gg})}} \times \exp\left\{-\frac{1}{2}[\hat{C}_L^{gg} - C_L^{gg}(b)] (\text{Cov}_{LL'}^{gg})^{-1} [\hat{C}_L^{gg} - C_L^{gg}(b)]\right\}, \quad (30)$$

where  $N_L = 7$  is the number of multipole bins and  $\text{Cov}_{LL'}^{gg}$  is the covariance matrix computed as described in subsection 4.2.

Sampling this likelihood for the measured H-ATLAS galaxy power spectrum  $\hat{C}_L^{gg}$  we obtained constraints on the galaxy bias. Estimated values of the bias for all patches as well as for each of them are presented in Table 3. The results for the different patches are consistent with each other within  $\lesssim 2\sigma$ . The global value,  $b = 2.84 \pm 0.12$ , is consistent with earlier estimates. For example Xia et al. (2012) found an effective value of the bias factor  $b_{\text{eff}} \simeq 3$  (no error given) “for the bulk of galaxies at  $z \simeq 2$ ”. Planck Collaboration XXX (2014) found, from their analysis of the CIB, a slightly lower value ( $b_{\text{eff}} \simeq 2.6$ ), as expected since a large contribution to the CIB comes from fainter, presumably less biased, sources.

We used the measured cross-spectra to constrain the  $b$  and  $A$  parameters in the same fashion. As noted above, the cross-spectra basically measure the product  $A \times b$ .

The likelihood function is given by:

$$\mathcal{L}(\hat{C}_L^{\kappa g}|b, A) = \frac{1}{\sqrt{(2\pi)^{N_L} \det(\text{Cov}_{LL'}^{\kappa g})}} \times \exp\left\{-\frac{1}{2}[\hat{C}_L^{\kappa g} - A C_L^{\kappa g}(b)] (\text{Cov}_{LL'}^{\kappa g})^{-1} [\hat{C}_L^{\kappa g} - A C_L^{\kappa g}(b)]\right\}, \quad (31)$$

where  $\text{Cov}_{LL'}^{\kappa g}$  is the covariance matrix (eq. (21)). The results are shown in Table 3.

Finally, we studied the constraints on  $b$  and  $A$  by combining the cross- and galaxy auto-spectra. For the joint analysis we used the Gaussian likelihood function that takes into account correlations between the cross- and the auto-power spectra in the covariance matrix. We organized the extracted cross- and auto-bandpowers into a single data vector as

$$\hat{\mathbf{C}}_L = (\hat{C}_L^{\kappa g}, \hat{C}_L^{gg}), \quad (32)$$

which has 14 elements. The total covariance matrix is then written as the composition of four  $7 \times 7$  sub-matrices

$$\text{Cov}_{LL'} = \begin{bmatrix} \text{Cov}_{LL'}^{\kappa g} & (\text{Cov}_{LL'}^{\kappa g-gg})^\top \\ \text{Cov}_{LL'}^{\kappa g-gg} & \text{Cov}_{LL'}^{gg} \end{bmatrix} \quad (33)$$

where the mixed covariance which takes into account the correlation between the two observables is:

$$\begin{aligned} \text{Cov}_{LL'}^{\kappa g-gg} &= M_{LL_1}^{-1} P_{L_1 \ell} \widetilde{\text{Cov}}_{\ell \ell'}^{\kappa g-gg} Q_{\ell' L_2} (M_{L' L_2}^{-1})^\top \quad (34) \\ \widetilde{\text{Cov}}_{\ell \ell'}^{\kappa g-gg} &= \frac{2}{2\ell' + 1} \times \\ &\times M_{\ell \ell'} [(C_\ell^{gg}(b) + N_\ell^{gg})(C_{\ell'}^{gg}(b) + N_{\ell'}^{gg}) C_\ell^{\kappa g}(b) C_{\ell'}^{\kappa g}(b)]^{1/2} \quad (35) \end{aligned}$$

In the above expressions  $\text{Cov}_{LL'}^{\kappa g}$  and  $\text{Cov}_{LL'}^{gg}$  are the covariance matrices evaluated using eq. (21).

The full 2-dimensional posterior distributions of the  $b$  and  $A$  parameters, as well as the marginalized ones obtained from this analysis, are shown in Fig. 12. Numerical values of the parameters are presented in Table 3 where the best-fit values and the errors are evaluated as the 50<sup>th</sup>, 16<sup>th</sup>, and 84<sup>th</sup> percentiles, respectively, of the posterior distributions. The  $\chi^2$  values are evaluated as  $\chi_{\text{th}}^2 = [\hat{C}_L^{\kappa g} - A_{\text{bf}} \mathbf{C}_L^{\kappa g}(b_{\text{bf}})] (\text{Cov}_{LL'}^{\kappa g})^{-1} [\hat{C}_L^{\kappa g} - A_{\text{bf}} \mathbf{C}_L^{\kappa g}(b_{\text{bf}})]$ , where  $b_{\text{bf}}$  and  $A_{\text{bf}}$  are the best-fit values. Note that the posterior distributions of  $b$  and  $A$  obtained using only cross-correlation data are far from being Gaussian. As a sanity check we derived a theoretical upper limit on  $A$  considering that cross-spectrum cannot be larger than the geometric mean of the two auto spectra:  $A \leq (C_L^{\kappa g, \text{th}} (\text{Cov}_{LL'}^{\kappa g})^{-1} \sqrt{\hat{C}_L^{\kappa \kappa} \hat{C}_L^{gg}}) / (C_L^{\kappa g, \text{th}} (\text{Cov}_{LL'}^{\kappa g})^{-1} C_L^{\kappa g, \text{th}}) \sim 2.5$ .

The  $\chi^2$  value of the best-fit theoretical spectrum is  $\chi_{\text{th}}^2 = 12.6$  for  $\nu = 5$  degrees of freedom ( $\chi_{\text{th}}^2/\nu = 2.5$ ). The significance of the detection of the theoretically expected cross-correlation signal was evaluated as the ratio between the estimated amplitude  $A$  and its error  $\sigma_A$ :  $A/\sigma_A \simeq 10$ , corresponding to a  $10\sigma$  significance.

The constraint on the bias factor from the joint fit of the galaxy auto-correlation and of the cross-correlation

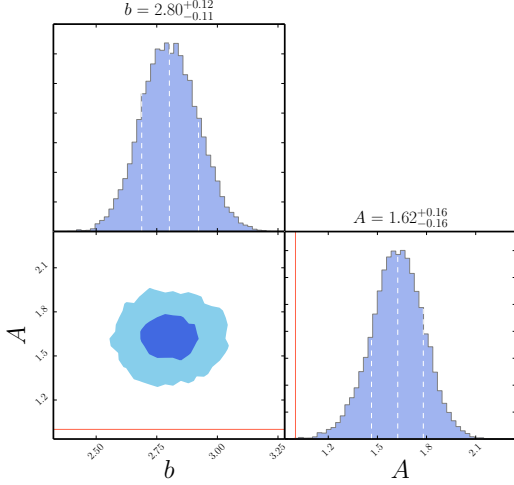


**Figure 12.** Posterior distribution in the  $b - A$  plane with the 68% and 95% confidence contours (darker and lighter colour, respectively), together with the marginalized distributions of each parameter with  $1\sigma$  errors shown by the dashed white lines, obtained combining the convergence-galaxy cross-correlation and the galaxy auto-correlation data for each patch. The solid red line represents the standard case in which  $A = 1$  while  $\alpha$  is set to 3 for the analysis.

power spectra,  $b = 2.80_{-0.11}^{+0.12}$ , is consistent with earlier estimates (Xia et al. 2012). On the other hand, the cross-correlation amplitude is  $A = 1.62 \pm 0.16$  times larger than expected for the standard  $\Lambda$ CDM model for the evolution of large-scale structure. This is at odds with the results of the cross-correlation analyses presented in the Planck Collaboration XVII (2013) paper, which are consistent with  $A = 1$  except, perhaps, in the case of the MaxBCG cluster catalog. Possible causes of the large value of  $A$  are discussed in the following section.

## 7. DISCUSSION

The correlation between the CMB lensing potential and the distribution of high- $z$ , sub-mm selected galaxies was found to be stronger than expected for the standard cosmological model. We now address on one side the possibility that the tension between the estimated and the expected value of the amplitude  $A$  is overrated because of an underestimate of the errors and, on the other side, astrophysical effects that may enhance the measured signal.

### 7.1. Noise levels

Due to the inhomogeneity of the noise level in the *Planck* survey, the H-ATLAS patches used for the cross-correlation may have slightly higher than average effective noise. To check this possibility we reconstructed the CMB convergence auto-power spectrum for each of the H-ATLAS patches. Error bars were derived from 100 simulated *Planck* lensing maps. The results of the analysis performed combining the five patches show some excess power for  $\ell \sim 400 - 500$  (Fig. 13). Considering the patches separately we find that the main features of the CMB lensing power spectrum are recovered in the two largest patches, while the power spectrum in the three GAMA fields seems to be dominated by noise. Thus there is an indication of a slight underestimate of the noise bias in the latter fields, but the effect on the combined patches is marginal.

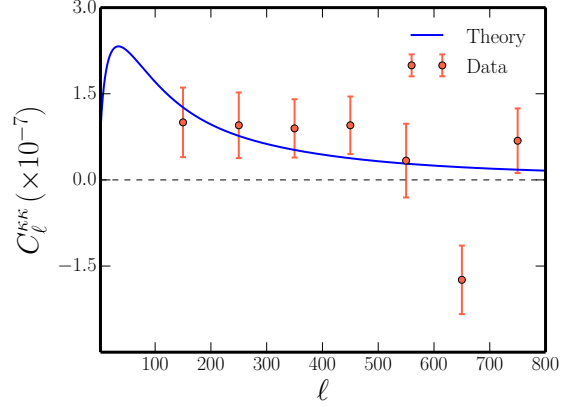


**Figure 13.** CMB convergence auto-power spectrum recovered using the H-ATLAS mask. Theory line as in Fig. 3.

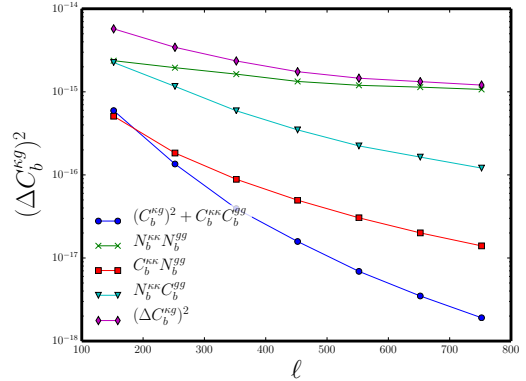


**Figure 14.** Contributions to the cross-spectrum variance  $(\Delta C_\ell^{\kappa g})^2$  [see eq. (36)]. Blue line: signal only term. Green line: noise only term. Red and cyan lines: mixed signal and noise terms.

To understand which is the main statistical error source on the cross-power spectrum we have analyzed the contributions to the error budget. The auto-spectra contain a signal and a noise term as  $\hat{C}_L^{XX} = C_L^{XX} + N_L^{XX}$ , so that the errors on the cross-spectra can be written as

$$f_{\text{sky}}(2L+1)\Delta\ell(\Delta\hat{C}_L^{\kappa g})^2 = [C_L^{\kappa\kappa}C_L^{gg} + (C_L^{\kappa g})^2] + N_L^{\kappa\kappa}N_L^{gg} + C_L^{\kappa\kappa}N_L^{gg} + C_L^{gg}N_L^{\kappa\kappa}. \quad (36)$$

The first term represents the cosmic variance, the second one the pure noise and the remaining are mixed signal-noise terms. As can be seen from Fig. 14, the main contribution to the  $C_L^{\kappa g}$  variance is given by the noise only term. Moreover, the relative amplitude of the mixed terms is telling us that most of the error comes from the lensing noise. In order to reduce the errors of the reconstructed cross-spectrum, it is important to reach high-sensitivity in reconstructing the CMB lensing potential. This, of course, does not include the possible systematic errors discussed below.

### 7.2. Astrophysical systematics

First we have checked the effect on the auto- and cross-spectra of errors of photometric redshift estimates. To this end we have redone the full analysis using the

**Table 3**  
H-ATLAS galaxy linear bias and cross-correlation amplitude as determined using both separately and jointly the reconstructed galaxy auto- and cross-spectra in the different patches.

Patch	$gg$		$\kappa g$		$\kappa g + gg$		$\chi^2_{\text{th}}/\nu$	p-value
	$b$		$b$	$A$	$b$	$A$		
ALL	$2.84^{+0.12}_{-0.11}$		$8.66^{+4.23}_{-4.37}$	$0.63^{+0.52}_{-0.20}$	$2.80^{+0.12}_{-0.11}$	$1.62^{+0.16}_{-0.16}$	12.6/5	0.03
NGP	$2.72^{+0.22}_{-0.21}$		$7.92^{+5.38}_{-6.38}$	$0.53^{+1.35}_{-0.26}$	$2.75^{+0.22}_{-0.21}$	$1.27^{+0.28}_{-0.29}$	23.1/5	$3 \times 10^{-4}$
SGP	$2.67^{+0.19}_{-0.19}$		$0.78^{+1.86}_{-0.61}$	$3.48^{+2.63}_{-1.95}$	$2.69^{+0.18}_{-0.18}$	$1.56^{+0.23}_{-0.23}$	5.7/5	0.34
G09	$3.79^{+0.35}_{-0.37}$		$8.99^{+4.02}_{-5.06}$	$1.11^{+0.96}_{-0.36}$	$3.72^{+0.35}_{-0.32}$	$2.11^{+0.41}_{-0.41}$	6.9/5	0.22
G12	$3.43^{+0.35}_{-0.33}$		$3.34^{+6.84}_{-2.55}$	$2.04^{+3.41}_{-1.23}$	$3.36^{+0.35}_{-0.33}$	$2.05^{+0.47}_{-0.46}$	13.7/5	0.02
G15	$3.14^{+0.33}_{-0.35}$		$8.57^{+4.85}_{-6.54}$	$0.97^{+1.72}_{-0.38}$	$3.13^{+0.34}_{-0.34}$	$2.06^{+0.45}_{-0.47}$	18.4/5	$2 \times 10^{-3}$

initial redshift distribution,  $dN/dz$ , i.e. the one represented by the dashed red line in Fig. 4. We get a slightly higher value of the cross-spectrum amplitude ( $A = 1.70^{+0.16}_{-0.17}$ ) and a somewhat lower value of the galaxy bias ( $b = 2.59^{+0.11}_{-0.11}$ ). The reason for that is easily understood. As shown by Fig. 4, the convolution of the initial  $dN/dz$  with the smoothing kernel (representative of the uncertainties on estimated redshifts) results in a broadening of the distribution. This translates in a decrease of the expected amplitude for both the cross- and the auto-power spectra. Hence, in order to fit the same data, we need a higher value of the galaxy bias and, consequently, a lower value of the cross-spectrum amplitude  $A$ . Since the derived value of  $b$  is quite sensitive to the adopted redshift distribution, the agreement with other, independent determinations implies that our  $dN/dz$  cannot be badly off. Therefore it looks unlikely that the higher than expected value of  $A$  can be ascribed to a wrong estimate of  $dN/dz$ .

Our choice of a constant  $b$  over the redshift range spanned by the H-ATLAS catalogue is obviously an approximation and the effective values of  $b$  may be different for the cross- and the galaxy auto-power spectra. To check the effect of this approximation on the estimates of  $C_{\ell}^{\kappa g}$  and  $C_{\ell}^{gg}$  we have computed the effective values of the bias for the two cases

$$b_{\text{eff}}^{\kappa g} = \frac{\int \frac{dz}{c} b(z) \frac{H(z)}{\chi^2(z)} W^{\kappa}(z) \frac{dN}{dz} P(k, z)}{\int \frac{dz}{c} \frac{H(z)}{\chi^2(z)} W^{\kappa}(z) \frac{dN}{dz} P(k, z)}, \quad (37)$$

$$(b_{\text{eff}}^{gg})^2 = \frac{\int \frac{dz}{c} b^2(z) \frac{H(z)}{\chi^2(z)} \left(\frac{dN}{dz}\right)^2 P(k, z)}{\int \frac{dz}{c} \frac{H(z)}{\chi^2(z)} \left(\frac{dN}{dz}\right)^2 P(k, z)},$$

using the bias evolution model  $b(z)$  from Sheth & Tormen (1999) for halo masses in the range  $10^{12}$ – $10^{13} M_{\odot}$ . We find that  $b_{\text{eff}}^{\kappa g}$  is only slightly larger (by  $\simeq 6\%$ ) than  $b_{\text{eff}}^{gg}$ . Hence, considering a redshift-dependent bias factor would only marginally affect the expected cross-spectrum.

Weak lensing by foreground structures modifies the *observed* density of background sources compared to the real one (magnification bias; Ho et al. 2008; Xia et al. 2009) and is especially important for high redshift objects. The effect on the galaxy over-density kernel is described by the second term on the right-side of eq. (6). The effect of the magnification bias on both  $C_{\ell}^{\kappa g}$  and  $C_{\ell}^{gg}$  is illustrated in Fig. 15 where we show the expected

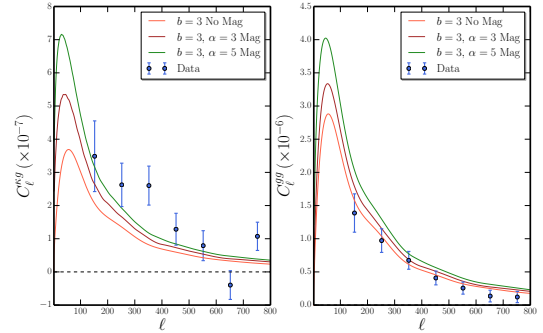


**Figure 15.** Effect of lensing magnification bias on the cross-power spectrum (left panel) and on the galaxy auto-power spectrum (right panel). In both panels theory lines are plotted for bias values  $b = 3$ , while the slope of the galaxy number counts as function of flux is set to  $\alpha = 1$  (no magnification) and  $\alpha = 3, 5$  as described in the legend.

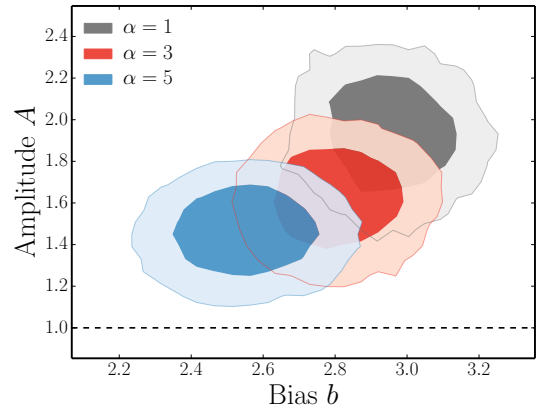


**Figure 16.** Effect of fixed slope of number counts  $\alpha$  on the inferred values of cross-correlation amplitude  $A$  and bias  $b$ . We show 1- and 2 $\sigma$  contours (darker and lighter shaded regions respectively). As the  $\alpha$  parameter increases, both  $A$  and  $b$  shift towards smaller values.

power spectra for  $A = 1$ ,  $b = 3$  and three values of  $\alpha$ : 1 (no magnification bias), 3, and 5. The impact of the magnification bias is clearly stronger for  $C_{\ell}^{\kappa g}$ .

Fitting the joint data for  $\alpha = 1$  we find  $b = 2.95^{+0.12}_{-0.11}$  and  $A = 1.93^{+0.18}_{-0.19}$  while for  $\alpha = 5$   $b = 2.55^{+0.13}_{-0.12}$  and  $A = 1.46 \pm 0.14$ . The contour plots in the  $A$ – $b$  plane are shown in Fig. 16. Higher values of  $\alpha$  imply lower values of  $A$ , but even for  $\alpha = 5$  the data require  $A > 1$ .

Another systematic effect that can bias our measurement of the CMB convergence-galaxy cross-correlation is

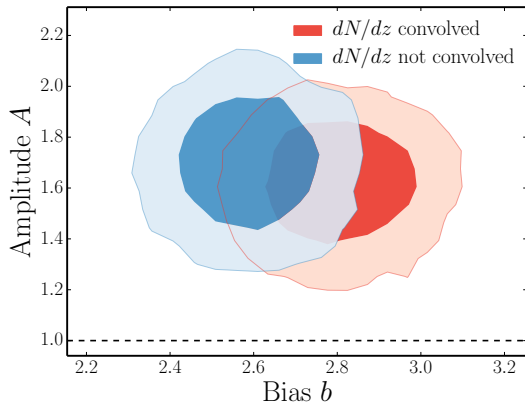


**Figure 17.** Posterior distributions for  $A$  and  $b$  obtained using the convolved (red contours) and the unconvolved  $dN/dz$  (blue contours).

the leakage of cosmic infrared background (CIB) emission into the lensing map through the temperature maps used for the lensing estimation, as it correlates strongly with the CMB lensing signal (Planck Collaboration XVIII 2013). The 853 GHz *Planck* map used by Planck Collaboration XVII (2013) as a Galactic dust template also removes the portion of the CIB fluctuations which have a spectral index similar to that of Galactic dust. However, as noted in that paper, this approach is liable to problems due, e.g., to variation of Galactic dust spectral indices across the sky as well as to the mismatch between the beams at 100/143/217 and 857 GHz.

The H-ATLAS galaxies are well below the *Planck* detection limits (their flux densities at 148 GHz are expected to be in the range 0.1–1 mJy, hence are much fainter than sources masked by Planck Collaboration XVII 2013). Thus they are part of the CIB measured by *Planck*. If they are only partially removed by the use of the 857 GHz map they are potentially an important contaminant of the cross-correlation, resulting in an enhancement of the observed signal. The shot-noise correction applied by the *Planck* team removes only partly the contamination by infrared sources since their main contribution to the fluctuation field is due to clustering.

Estimates of biases to the lensing reconstruction signal from extragalactic sources have been worked out by the Osborne et al. (2014); van Engelen et al. (2014). However a calculation of the bias on the cross-spectrum discussed in this paper is beyond the scope of the present paper. We expect that with the next release of the *Planck* data, CMB lensing maps at different frequencies will become available. This will allow us to investigate the CIB leakage issue in more detail.

Clusters of galaxies, which trace the large scale potential responsible for the CMB lensing, are visible at mm and sub-mm wavelengths via the scattering of CMB photons by hot electrons (Sunyaev-Zel’dovich effect) and might therefore contaminate the cross-correlation signal to some extent. However, the redshift range populated by galaxy clusters only marginally overlaps with the redshift distribution of our sources, so that this contamination is negligible.

## 8. SUMMARY AND CONCLUSIONS

We have presented the first measurement of the correlation between the lensing potential derived from the

*Planck* data and a high- $z$  ( $z \geq 1.5$ ) galaxy catalogue from the *Herschel*-ATLAS survey, the highest redshift sample for which the correlation between *Planck* CMB lensing and tracers of large-scale structure has been investigated so far. We have shown that the expected signal is remarkably strong, in spite of the small area covered by the H-ATLAS survey (about 1.3% of the sky), suggesting that cross-correlation measurements between CMB lensing maps and galaxy surveys can provide powerful constraints on evolution of density fluctuations, on the nature of the dark energy, and on properties of tracers of the matter distribution, provided that a good control of systematic errors for both data sets can be achieved.

The null hypothesis (no correlation) was rejected with a significance of about  $20\sigma$  and the significance of the detection of the theoretically expected cross-correlation signal was found to be  $10\sigma$ . The reliability of this result was confirmed by several null tests. A joint analysis of the cross-spectrum and of the auto-spectrum of the galaxy density contrast yielded a galaxy bias parameter  $b = 2.80^{+0.12}_{-0.11}$ , consistent with earlier estimates for H-ATLAS galaxies at similar redshifts. On the other hand, the amplitude of the cross-correlation was found to be a factor  $1.62 \pm 0.16$  higher than expected from the standard model and found by cross-correlation analyses with other tracers of the large-scale structure.

We have investigated possible reasons for the excess amplitude. Some of them, such as the redshift dependence of the bias parameter or the contamination by the Sunyaev-Zeldovich effect, were found to be negligible. Others, such as the magnification bias due to weak gravitational lensing or errors in the photometrically estimated redshifts, can contribute significantly to the observed excess but cannot fully account for it. A possible culprit is some residual contamination of convergence maps by unresolved infrared sources (Osborne et al. 2014; van Engelen et al. 2014), adding a substantial contribution to the measured correlation between the lensing convergence and the H-ATLAS high- $z$  sources, which are unresolved by *Planck*. However a detailed calculation of this effect is complicated and beyond the scope of the present paper.

We have also investigated the possibility that the tension between the observed and the expected cross-correlation amplitude was overrated because the noise level of the convergence maps in the regions used for the cross correlation is above typical values. This turned out to be the case in the three GAMA fields, but the effect on the combination of fields was found to be marginal.

An exquisite mapping of the CMB lensing pattern is one of the major goals of operating and planned CMB probes, because of its relevance in studying cosmological structure formation and the properties of the dark energy. Forthcoming data releases by *Planck* as well as future CMB lensing measurements from sub-orbital probes will be most relevant to further address the results presented here and improve the constraining power of these studies, both in a cosmological and astrophysical context.

We thank Karim Benabed and Laurence Perotto for useful discussions and comments, Duncan Hanson and Michal Michalowski for a careful reading of the paper and the anonymous referee for insightful comments that

helped us improving the paper. FB would like to thank Simone Aiola, Matteo Calabrese and Giulio Fabbian for stimulating discussions. CB thanks Andrew Jaffe and Radek Stompor for useful discussions. We gratefully acknowledge support from INAF PRIN 2012/2013 "Looking into the dust-obscured phase of galaxy formation through cosmic zoom lenses in the Herschel Astrophysical Terahertz Large Area Survey", and from ASI/INAF agreement 2014-024-R.0. FB acknowledges partial support from the INFN-INDARK initiative. LD, RJI and SM acknowledge support from the European Research Council (ERC) in the form of Advanced Investigator Program, COSMICISM. JGN acknowledges financial support from the Spanish CSIC for a JAE-DOC fellowship, co-funded by the European Social Fund. The work has been supported in part by the Spanish Ministerio de Ciencia e Innovacion, AYA2012-39475-C02-01, and Consolider-Ingenio 2010, CSD2010-00064, projects. The authors acknowledge the use of CAMB and HEALPix packages and of the *Planck* Legacy Archive (PLA). A.L. thanks SISSA for warm hospitality.

## REFERENCES

- Antolini, C., Fantaye, Y., Martinelli, M., et al. 2014 *J. Cosmology Astropart. Phys.*1402, 039
- Bartelmann, M., & Schneider, P. 2001, *Phys. Rep.*, 340, 291
- Béthermin, M., Le Floch, E., Ilbert, O., et al. 2012, *A&A*, 542, A58
- Bleem, L. E., van Engelen, A., Holder, G. P., et al. 2012, *ApJL*, 753, L9
- Brown, M. L., Castro, P. G., & Taylor, A. N. 2005, *MNRAS*, 360, 1262
- Cai, Z.-Y., Lapi, A., Xia, J.-Q., et al. 2013, *ApJ*, 768, 21
- Das, S., Louis, T., Nolta, M. R., et al. 2014, *J. Cosmology Astropart. Phys.*, 4, 14
- Das, S., Sherwin, B. D., Aguirre, P., et al. 2011, *Physical Review Letters*, 107, 021301
- Dunne, L., Gomez, H., da Cunha, E., et al. 2011, *MNRAS*, 417, 1510
- Eales, S., Dunne, L., Clements, D., et al. 2010, *PASP*, 122, 499
- Feng, C., Aslanyan, G., Manohar, A. V., et al. 2012, *Phys. Rev. D*, 86, 063519
- Foreman-Mackey, D., Hogg, D. W., Lang, D., & Goodman, J. 2013, *PASP*, 125, 306
- Geach, J. E., Hickox, R. C., Bleem, L. E., et al. 2013, *ApJL*, 776, L41
- González-Nuevo, J., Lapi, A., Fleuren, S., et al. 2012, *ApJ*, 749, 65
- González-Nuevo, J., Lapi, A., Negrello, M., et al. 2014, *MNRAS*, 442, 2680
- Goodman, J., & Weare, J. 2010, *Comm. App. Math. Comp. Sci.*, 5, 65
- Górski, K. M., Hivon, E., Banday, A. J., et al. 2005, *ApJ*, 622, 759
- Griffin, M. J., Abergel, A., Abreu, A., et al. 2010, *A&A*, 518, L3
- Guo, Q., Cole, S., Lacey, C. G., et al. 2011, *MNRAS*, 412, 2277
- SPTpol Collaboration, D. Hanson et al. 2013, *Phys. Rev. Lett.*, 111 14, 141301
- Hauser, M. G., & Peebles, P. J. E. 1973, *ApJ*, 185, 757
- Hirata, C. M., Ho, S., Padmanabhan, N., Seljak, U., & Bahcall, N. A. 2008, *Phys. Rev. D*, 78, 043520
- Hirata, C. M., & Seljak, U. 2003, *Phys. Rev. D*, 67, 043001
- Hivon, E., Górski, K. M., Netterfield, C. B., et al. 2002, *ApJ*, 567, 2
- Ho, S., Hirata, C., Padmanabhan, N., Seljak, U., & Bahcall, N. 2008, *Phys. Rev. D*, 78, 043519
- Holder, G. P., Viero, M. P., Zahn, O., et al. 2013, *ApJL*, 771, L16
- Hu, W. 2000, *Phys. Rev. D*, 62, 043007
- Hu, W., & Okamoto, T. 2002, *ApJ*, 574, 566
- Ibar, E., Ivison, R. J., Cava, A., et al. 2010, *MNRAS*, 409, 38
- Kamionkowski, M., Kosowsky, A., & Stebbins, A. 1997, *Phys. Rev. D*, 55, 7368
- Keisler, R., Reichardt, C. L., Aird, K. A., et al. 2011, *ApJ*, 743, 28
- Lapi, A., González-Nuevo, J., Fan, L., et al. 2011, *ApJ*, 742, 24
- Lewis, A., & Challinor, A. 2006, *Phys. Rep.*, 429, 1
- Lewis, A., Challinor, A., & Lasenby, A. 2000, *ApJ*, 538, 473
- Limber, D. N. 1953, *ApJ*, 117, 134
- Maddox, S. J., Dunne, L., Rigby, E., et al. 2010, *A&A*, 518, L11
- Osborne, S. J., Hanson, D., & Doré, O. 2014, *J. Cosmology Astropart. Phys.*, 3, 24
- Pascale, E., Auld, R., Dariush, A., et al. 2011, *MNRAS*, 415, 911
- Pilbratt, G. L., Riedinger, J. R., Passvogel, T., et al. 2010, *A&A*, 518, L1
- Planck Collaboration, Ade, P. A. R., Aghanim, N., et al. 2014, *A&A*, 571, A1
- Planck Collaboration, Ade, P. A. R., Aghanim, N., et al. 2014, *A&A*, 571, A16
- Planck Collaboration, Ade, P. A. R., Aghanim, N., et al. 2013, *A&A*, 571, A17
- Planck Collaboration, Ade, P. A. R., Aghanim, N., et al. 2014, *A&A*, 571, A18
- Planck Collaboration, Ade, P. A. R., Aghanim, N., et al. 2014, *A&A*, 571, AA30
- Poglitich, A., Waelkens, C., Geis, N., et al. 2010, *A&A*, 518, L2
- POLARBEAR Collaboration, Ade, P. A. R., et al. 2014 *Phys. Rev. Lett.*112, 131302
- Rigby, E. E., Maddox, S. J., Dunne, L., et al. 2011, *MNRAS*, 415, 2336
- Sherwin, B. D., Das, S., Hajian, A., et al. 2012, *Phys. Rev. D*, 86, 083006
- Sheth, R. K., & Tormen, G. 1999, *MNRAS*, 308, 119
- Smith, D. J. B., Dunne, L., Maddox, S. J., et al. 2011, *MNRAS*, 416, 857
- Smith, K. M., Zahn, O., & Doré, O. 2007, *Phys. Rev. D*, 76, 043510
- Smith, R. E., Peacock, J. A., Jenkins, A., et al. 2003, *MNRAS*, 341, 1311
- Y. S. Song, A. Cooray, L. Knox and M. Zaldarriaga 2003, *ApJ*, 590, 664
- van Engelen, A., Bhattacharya, S., Sehgal, N., et al. 2014, *ApJ*, 786, 13
- van Engelen, A., Keisler, R., Zahn, O., et al. 2012, *ApJ*, 756, 142
- Xia, J.-Q., Negrello, M., Lapi, A., et al. 2012, *MNRAS*, 422, 1324
- Xia, J.-Q., Viel, M., Baccigalupi, C., & Matarrese, S. 2009, *J. Cosmology Astropart. Phys.*, 9, 3